Seventh International Conferenceon Computational Fluid Dynamics (ICCFD7), Big Island, Hawaii, July 9-13, 2012

ICCFD7-1502

Numerical Simulation of Roughness Effect on the Stability of a Hypersonic Boundary Layer

K.D. Fong*, X. Wang* and X. Zhong*
Corresponding author: dannyfong@ucla.edu

* University of California at Los Angeles, USA

Abstract: Numerical simulation of two dimensional roughness effects on modal growth is conducted over a hypersonic boundary layer. The steady base flow is firstly simulated by solving compressible Navier-Stokes equations. Perturbation corresponds to Mode S at $100KHz$ and a wall normal velocity pulse which has a frequency range of $1\ MHz$ are imposed into the mean flow with roughness separately. FFT is used to study the evolution of perturbation at different frequency. Both one roughness case and two roughness case have been considered. It is found that when roughness is at a location corresponding to the synchronization point of a particular frequency (synchronization point frequency), perturbation at frequency higher than the synchronization point frequency is damped. On the other hand, perturbation at frequency lower than the synchronization point frequency is amplified by roughness. This result is consistent with our previous study in which roughness location is changed. The relation between roughness and synchronization point can be a candidate to explain roughness delay transition as shown by some experiments.

Keywords: Hypersonic Boundary Layer, Roughness, Cut-Cell Method, Transition, Receptivity

1. Introduction

Roughness induced transition has a great impact on the development of hypersonic vehicles[1]. For example, transition can have a first-order impact on the lift and drag, stability and control, and heat transfer properties of the vehicles [2]. Roughness induced transition is an important consideration in the design of thermal protection systems (TPS) of hypersonic vehicles [3, 4]. For a reentry vehicle entering earth's atmosphere, it initially experiences a heating environment associated with a laminar boundary layer. As the vehicle altitude decreases, the vehicle surface becomes rougher and the boundary layer becomes turbulent. The transition from a laminar boundary layer to a turbulent one leads to the increase of surface heating rates by a factor of five or more. Thus, the ability to understand the physics of roughness induced transition plays an essential role in the design of TPS for reentry vehicles. Currently, roughness induced laminar-turbulent transition in hypersonic boundary layers, especially that induced by arbitrary surface roughness, is still poorly understood due to the limitation in experimental facilities and numerical methods [5].

Ideally the laminar-turbulent transition process can be divided into four stages. The first stage involves small disturbance fields which are initialized via a process termed "receptivity" by the viscous flow. The initial disturbance fields can involve both free stream and vehicle self-induced fluctuations such as acoustics, dynamic vortices, entropy spottiness, etc. The next stage is the linear growth stage, where small disturbances are amplified until they reach certain amplitude where nonlinear effects become important. The amplification can be in the form of exponential growth of Eigen modes (Tollmien-Schlichting waves or Mack waves) and non-modal growth of optimal disturbances (Transient growth). Once a disturbance has reached finite amplitude, it often saturates and transforms the flow into a new, possibly unsteady

state, which is termed as the secondary instability stage. The last stage is the breakdown stage where nonlinearities and/or high-order instabilities excite an increasing number of scales and frequencies in the flow.

The receptivity study is mainly concerned with the excitation of instability waves, the characteristics of which can be analyzed by the linear stability theory (LST) [6]. The LST analyzes the propagation of individual sinusoidal waves in the streamwise direction inside the boundary layer. These waves are referred as Tollmien-Schlichting (T-S) waves for low speed flow, whose amplitudes vary though the boundary layer and die off exponentially outside the boundary layer. Extensive numerical and theoretical researches have been conducted to solve the linearized Navier-Stokes equations and many characteristics regarding the instability waves in hypersonic boundary layers have been discovered [6-10]. Mack [6] identified the unstable modes by using the LST for compressible flow. He showed that inside a supersonic boundary layer, there are multiple higher instability modes in addition to the first mode, which is the compressible counterpart of T-S waves in the incompressible boundary layers. These instability modes in the supersonic boundary layer are termed as first mode, second mode, third mode, etc. For supersonic boundary layer with Mach number larger than four, Mack's second mode is the most unstable mode, and it plays an important role in hypersonic boundary layer transition.

Direct numerical simulation has become an effective research tool for studying hypersonic boundary layer receptivity, stability, and transition by numerically solving the time-dependent three-dimensional Navier–Stokes equations for the temporally or spatially evolving instability waves. Malik et al. [11] investigated the responses of a Mach 8 flow over a sharp wedge of a half-angle of 5.3^{o} to three types of external forcing: a planar freestream acoustic wave, a narrow acoustic beam enforced on the bow shock near the leading edge, and a blowing-suction slot on the wedge surface. They concluded that these three types of forcing eventually resulted in the same type of instability waves in the boundary layer. Ma and Zhong[12] studied the receptivity mechanisms of the same hypersonic boundary layer to various freestream disturbances, i.e., fast and slow acoustic waves, vorticity waves, and entropy waves, by solving the two-dimensional compressible Navier-Stokes equations. They found that the stable modes in the boundary layer played a very important role in the receptivity process. Recently, Wang et al. [13] further studied the response of the Mach 8 flow over a 5.3^{o} half-angle sharp wedge to wall blowing–suction. The results showed that mode S is strongly excited when the actuator is located upstream of the corresponding synchronization point. There is no significant amplification of pressure perturbation when the actuator is downstream of the synchronization point. Although the exact cause and mechanism of this result were not clear, such a result was obtained for wall blowing–suction at all frequencies considered in their study. Balakumar[14] numerically investigated the receptivity of a 2-D roughness to acoustic waves and found the isolated roughness does not contribute much in generating unstable disturbances. Marxen et al. [15] simulated the effects of a localized two-dimensional roughness element on the disturbance amplification in a hypersonic boundary layer. Their numerical experiments showed that in the vicinity of the separation regions, which are located in the upstream and downstream of the roughness, an increased amplification of a second-mode disturbance occurs for a certain frequency.

Roughness has long been used to trip boundary layer to turbulence, but studies have been found that roughness is capable of stabilizing boundary layer as well. Back in 1964, Holloway and Sterrett [16] performed experiments on a boundary layer at Mach 4.0 and 6.0 with surface roughness at different local Reynolds number. They found that under certain circumstances, roughness with height less than boundary layer thickness can delay the transition onset on the flatplate compared with no roughness situation. However, no physical reasons had been given in the paper. Later, Fujii investigated the effect of two dimensional surface roughness on a hypersonic boundary layer[17]. The experiment was carried out at the JAXA 0.5m hypersonic wind tunnel using a 5 deg half angle sharp cone. It was found that wavy wall roughness can delay transition. Nevertheless, the exact cause of the delay is still unknown.

Previous DNS studies have shown that the roughness location plays an important role in the developments of mode S excited by the blowing-suction slot [18]. It is found that the location of synchronization point and roughness is important in deciding roughness effect [19]. Duan et al [19] shows that when roughness is placed downstream of the synchronization point of one mode, that mode will be damped by roughness. However, if roughness is placed upstream of the synchronization point, the mode will be amplified. This could lead to an explanation of roughness delay transition as shown by

experiments. [16, 17] Thus, providing a way to control transition using two dimensional roughness may be possible. In this paper, we further investigate the finite roughness effect on perturbation growth over a Mach 5.92 flat-plate boundary layer. To expand the study by Duan et al [19] and Fong et al [20], the unsteady simulation model in this paper are mode S perturbation and a wall normal velocity pulse. The wall normal velocity pulse has a frequency range of $1\,MHz$. The effect of roughness location and perturbation frequency is studied by FFT analysis. Moreover, the role of roughness height is also studied in mode S case.

2. Governing Equations

For direct numerical simulation of hypersonic boundary layer transition, the governing equations are the three-dimensional Navier–Stokes equations. We assume that we are dealing with Newtonian fluids with the perfect gas assumption and isothermal or adiabatic wall conditions. The governing equations can be written in the following conservation-law form in the Cartesian coordinates,

$$\frac{\partial U}{\partial t}+\frac{\partial F_j}{\partial x_j}+\frac{\partial F_{vj}}{\partial x_j}=0 \tag{1}$$

where U, F_j and F_{vj} are the vectors of flow variables, convective flux, and viscous flux in the *jth* spatial direction respectively, i.e.,

$$U=\left\{\rho,\rho u_1,\rho u_2,\rho u_3,e\right\} \tag{2}$$

$$F_j=\begin{Bmatrix}\rho u_j\\ \rho u_1u_j+p\delta_{1j}\\ \rho u_2u_j+p\delta_{1j}\\ \rho u_3u_j+p\delta_{1j}\\ (e+p)u_j\end{Bmatrix} \tag{3}$$

$$F_{vj}=\begin{Bmatrix}0\\ \tau_{1j}\\ \tau_{2j}\\ \tau_{3j}\\ \tau_{jk}u_k-q_j\end{Bmatrix} \tag{4}$$

In this paper, only perfect-gas hypersonic flow is considered, i.e.,

$$p=\rho RT \tag{5}$$

$$e=\rho(C_vT+\frac{1}{2}u_ku_k) \tag{6}$$

$$\tau_{ij}=\mu(\frac{\partial u_i}{\partial x_j}+\frac{\partial u_j}{\partial x_i})+\delta_{ij}\lambda\frac{\partial u_k}{\partial x_k} \tag{7}$$

$$q_j=-k\frac{\partial T}{\partial x_j} \tag{8}$$

where R is the gas constant. The specific heat C_v is assumed to be constant with a given ratio of specific heats γ. The viscosity coefficient μ can be calculated by Sutherland's law in the form:

$$\mu = \mu_r \left(\frac{T}{T_0} \right)^{3/2} \frac{T_0 + T_s}{T + T_s} \tag{9}$$

where, for air, $\mu_r = 1.7894 \times 10^{-5} Ns/m^2, T_0 = 288.0K, T_s = 110.33K$ and λ is assumed to be $-2/3\mu$. The heat conductivity coefficient k can be computed through a constant Prantl number.

3. High Order Cut-Cell Method

A schematic of a computational domain and a cut-cell grid in roughness induced hypersonic boundary layer transition is shown in Figure 1. This figure shows a typical hypersonic flow over a blunt body, where a bow shock is created by the supersonic freestream. In this paper, a high-order shock-fitting method is used to track the movement of the bow shock which is treated as the upper boundary of the computational domain. The computational grid for a shock-fitting formulation is bounded between the bow shock above and the blunt body below. The cut-cell grid is a smooth curvilinear grid fitted to the baseline body shape without the roughness. As a result, the roughness surface cuts across the grid lines. The roughness surface, Γ, is represented by surface equation in the following form,

$$\Gamma : f(x, y, z) = 0 \tag{10}$$

For a problem concerning practical arbitrary roughness, it is likely that there is no analytical equation applicable to represent the shape of the roughness element. In this case, a set of n discrete points $\{(x_1, y_1, z_1), (x_2, y_2, z_2), ..., (x_n, y_n, z_n)\}$ are used to represent the surface.

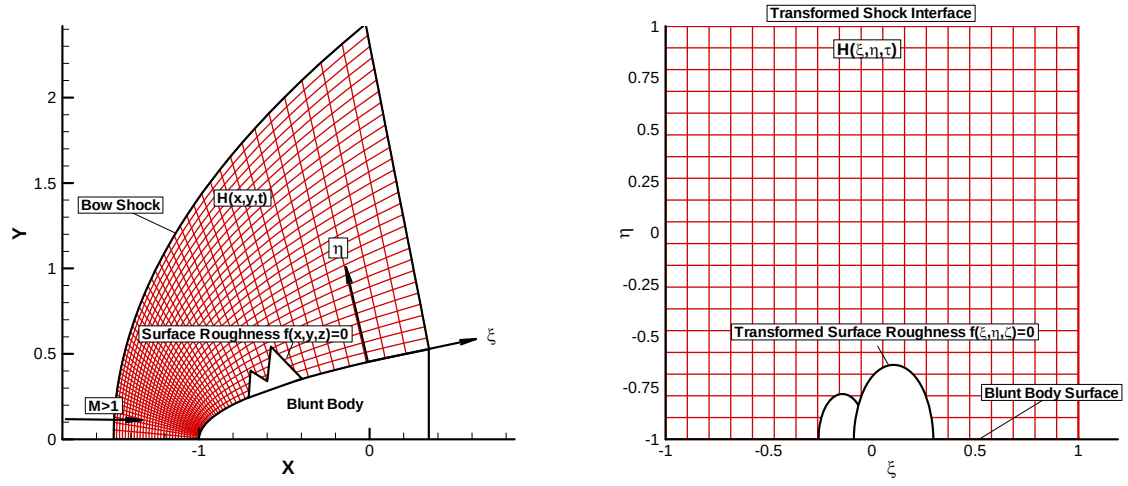

(a) **(b)**

Figure 1.Physical and computational domain and a cut-cell grid of hypersonic flow over a blunt body with surface roughness: (a) physical grid, (b) computational grid with a transformed roughness

Both the governing Eq. (1) and the roughness equation (10) in the physical domain are transformed into a Cartesian computational domain bounded by bow shock and flat plate. Under the computational

coordinate system, the body fitted grids are represented by a curvilinear three-dimensional coordinates (ξ,η,ς) along the grid lines. The unsteady movement of the bow shock is treated as the computational upper boundary located at $\eta=\eta_{\max}$, which is time dependent. The other grid lines $\xi=const$ and $\varsigma=const$ remains stationary during computations. The coordinate transformation is defined by:

$$\begin{cases}\xi=\xi(x,y,z)\\ \eta=\eta(x,y,z,t)\\ \varsigma=\varsigma(x,y,z)\\ \tau=t\end{cases}\leftrightarrow\begin{cases}x=x(\xi,\eta,\varsigma,\tau)\\ y=y(\xi,\eta,\varsigma,\tau)\\ z=z(\xi,\eta,\varsigma,\tau)\\ t=\tau\end{cases} \tag{11}$$

where (x,y,z,t) are the physical coordinates defined under Cartesian coordinate system.

A third-order accurate Cut-Cell method is used in current numerical simulation [21]. A set of uniformly distributed Cartesian grids can be generated in the computational domain where the grid distribution in the physical domain is not uniformly distributed. Because smooth body-fitted grids are generated in the regular computational domain without the roughness, some of the Cartesian grid cells may be cut by the roughness boundary, which leads to irregular Cartesian grid cells. More details of the grid structure are discussed in a previous paper [21].

4. Result and Discussion

4.1. Flow conditions and roughness model

We have applied the high order cut cell method to model an isolated roughness on the surface of a hypersonic flatplate. Both steady and unsteady flows with surface roughness are considered. The freestream condition is the same as those used in used in Maslov's experiment [7] as follows,

$$\begin{cases}P_r=0.72, R_\infty=\rho_\infty * u_\infty/\mu_\infty=13.2\times10^6/m\\ M_\infty=5.92, T_\infty=48.69K, P_\infty=742.76Pa\end{cases} \tag{12}$$

where M_∞, T_∞, P_∞, P_r, R_∞ are Mach number, temperature, pressure, Prandtl number and unit Reynolds number, respectively. The flat plate is assumed to be isothermal. The total length of the flat plate is about 1.69 m.

An isolated roughness element of smooth shape is placed on the surface of the flat plate. Motivated by Whiteheard's experiments [22], the shape of the surface roughness is chosen to be a two-dimensional bump, governed by the following elliptic equation,

$$\frac{(x-x_c)^2}{a^2}+\frac{y^2}{b^2}=h^2 \tag{13}$$

where the parameters a, b and h control roughness width and height. In our test cases, roughness width is fixed at 2 times local boundary layer thickness while the height ranges from 25% to 62.5% of local boundary layer thickness. In addition, x_c defines the location of the roughness center. The grid size is 241 points in streamwise direction and 121 points in wall-normal direction in each computational zone. A third-order cut-cell method is used to compute the two-dimensional viscous hypersonic flow over the flat plate with the roughness element. A coordinate transformation is employed to transform the physical domain into a rectangle computational domain with a set of Cartesian grid. The detail of the transformation can be found in Fong et al [20].

4.2. Steady Flow solution with surface roughness

As mentioned, the high order cut cell method is implemented to model the roughness. In order to study the effect of both roughness locations and roughness heights on a hypersonic flatplate, the roughness is placed at four different locations. In each location, four different roughness heights ranging from 25% to 62.5% of the local boundary layer thickness are considered. The locations of roughness are chosen according to the synchronization point of $100KHz$ modes that are imposed into the flow for unsteady simulations in the previous study [20]. The details of each test case are listed below,

Case 1: Roughness at far upstream of the synchronization point, x_r=0.1101 m; Local boundary layer thickness; δ= 1.448x10^{-3} m; Roughness height 0.25δ, 0.375δ, 0.5δ, 0.625δ

Case 2: Roughness at upstream of the synchronization point, x_r=0.185 m; Local boundary layer thickness δ=1.61x10^{-3} m; Roughness height 0.25δ, 0.375δ, 0.5δ, 0.625δ

Case 3: Roughness at the synchronization point, x_r=0.331 m; Local boundary layer thickness δ=2.82x10^{-3} m; Roughness height 0.25δ, 0.375δ, 0.5δ, 0.625δ

Case 4: Roughness at downstream of the synchronization point, x_r=0.410 m; Local boundary layer thickness δ=3.42x10^{-3} m; Roughness height 0.25δ, 0.375δ, 0.5δ, 0.625δ

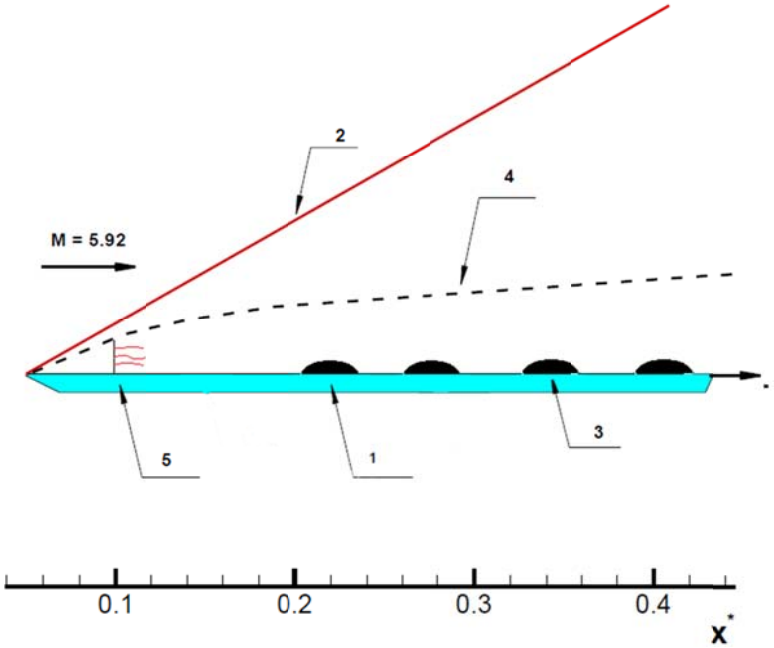

Figure 2.A schematic of the problem: 1. Roughness 2. Bow Shock 3. Synchronization point 4. Boundary layer 5. Pure Mode S or Mode F perturbation based on LST results, or pulse case.

Figure 2 shows the schematic of the numerical simulation. Figure 3 shows that pressure contour and streamline pattern for case 2 in which roughness is located at $x = 0.185m$. A strong compression region is observed upstream of roughness. Around the roughness, Mach waves are generated, and they travel downstream at an angle almost parallel to the shock. In the downstream vicinity of roughness, expansion waves can be seen. Moreover, streamline pattern shows that roughness introduces circulation in the vicinity around roughness. As Figure 3 shown, the size of such circulation is bigger in the upstream region of roughness. Bigger roughness also results a bigger circulation. Mach number contour is shown in Figure 4. It shows that roughness increases the Mach number boundary layer. Similar to the paper by

Klebanoff [23], we are interested in the region upstream and downstream of a roughness where the flow is distorted by the existence of the roughness. Figure 5 to Figure 8 shows the streamwise velocity profile upstream of roughness for case 2 with different roughness heights at different streamwise locations. The symbols in the figure represent the velocity profile for the case with roughness, while lines represent the profile for a flatplate without roughness. The figures clearly show that a bigger roughness not only increases boundary layer thickness. It also extends the size of region where one can 'feel' the existence of roughness. For example, the tallest roughness can affect of flow upstream at $x = 0.1446m$, while the shortest roughness can only have effect up to $x = 0.1671m$. The same trend is observed downstream of the roughness as shown in Figure 9 to Figure 12. For the shortest roughness case, the distortion is weak. The recovery zone only extends to $x = 0.21683m$. As the roughness gets bigger, the distortion gets stronger and the separation region becomes more obvious. The size of recovery zone consequentially becomes bigger. In our tallest roughness case, it extends to $x = 0.24135m$.

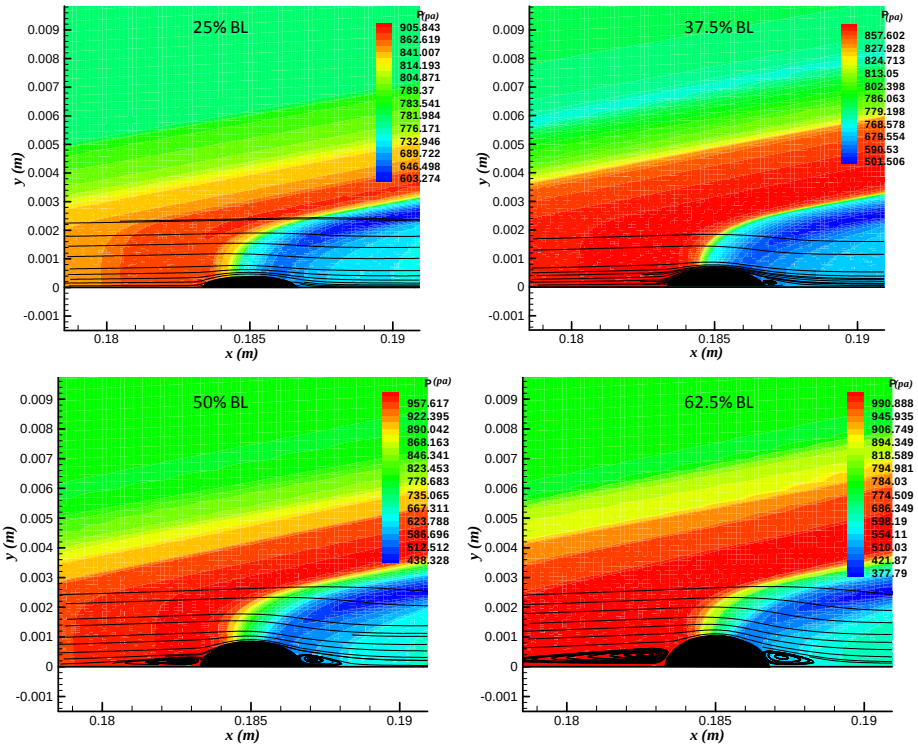

Figure 3. Pressure contour and streamline pattern around different roughness.

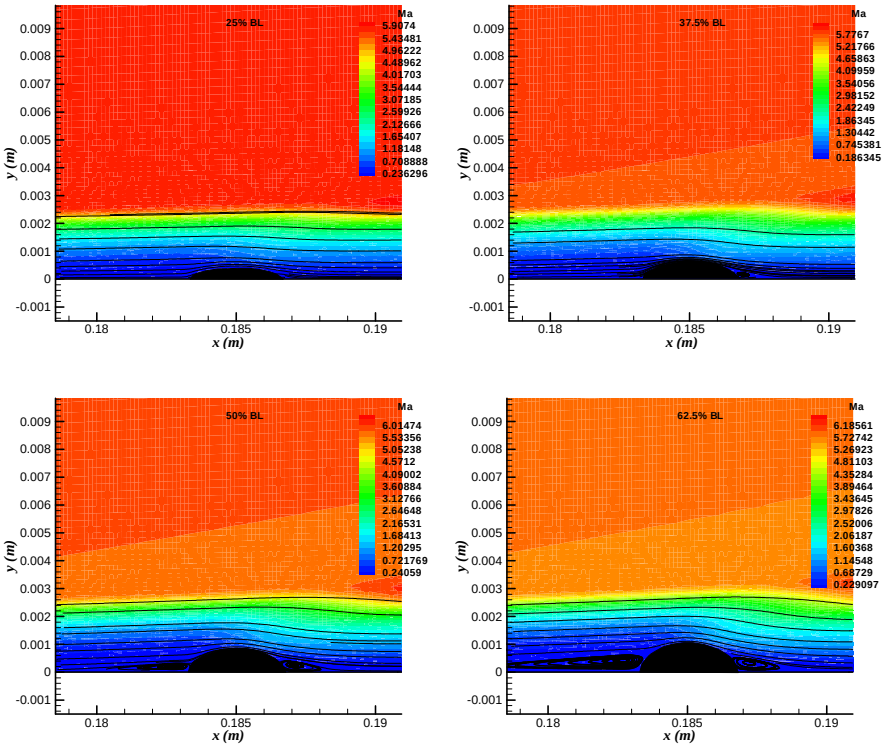

Figure 4. Mach number contour and streamline pattern around different roughness.

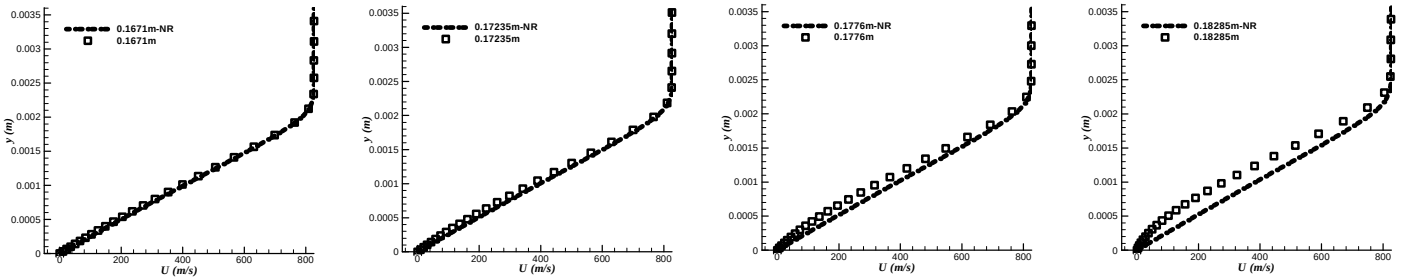

Figure 5.Streamwise velocity profile at different locations upstream of 25% roughness compared with no roughness case.

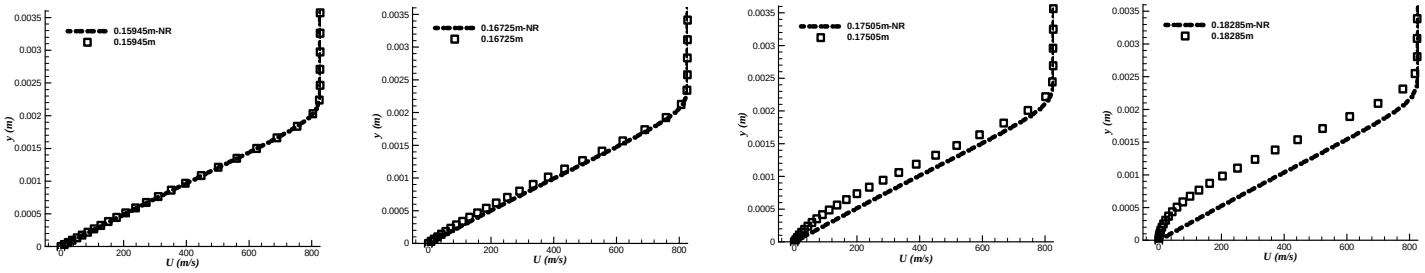

Figure 6.Streamwise velocity profile at different locations upstream of 37.5% roughness compared with no roughness case.

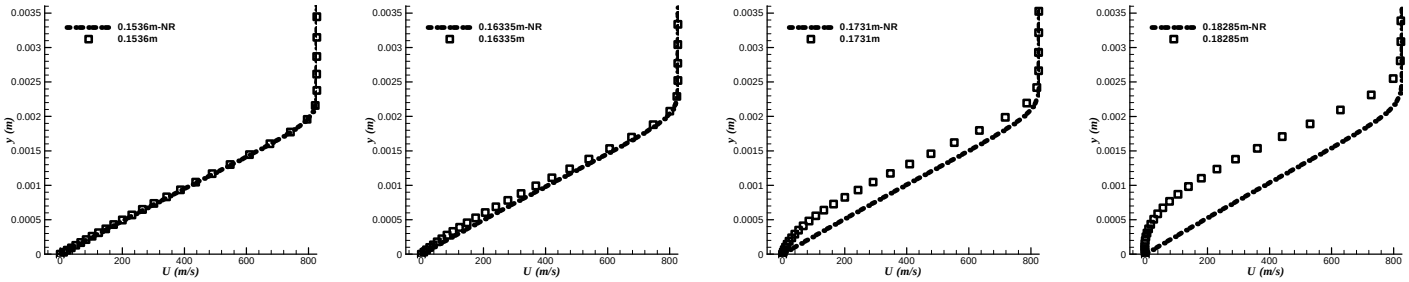

Figure 7.Streamwise velocity profile at different locations upstream of 50% roughness compared with no roughness case.

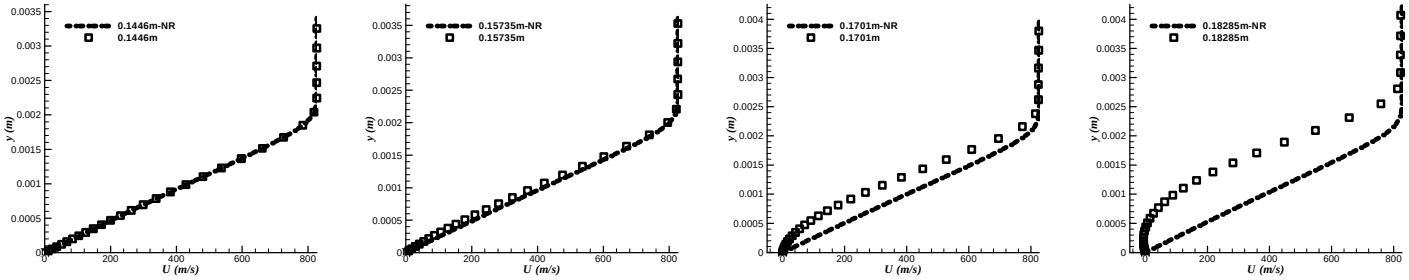

Figure 8.Streamwise velocity profile at different locations upstream of 62.5% roughness compared with no roughness case.

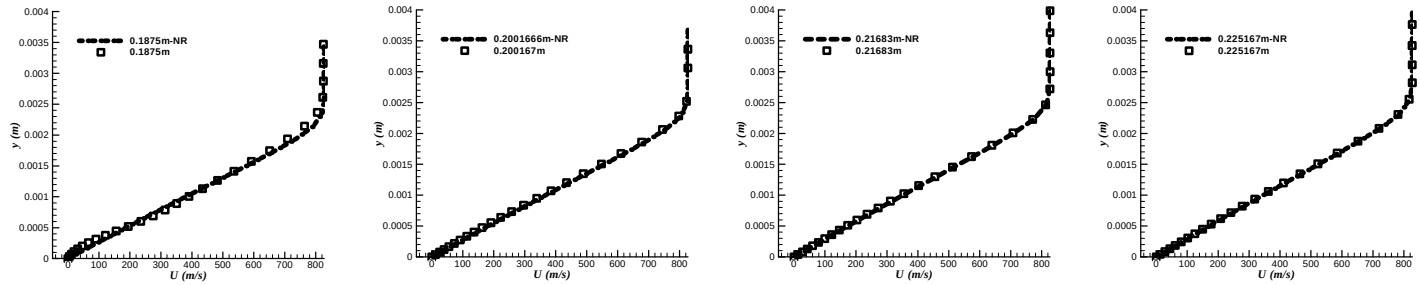

Figure 9.Streamwise velocity profile at different locations downstream of 25% roughness compared with no roughness case.

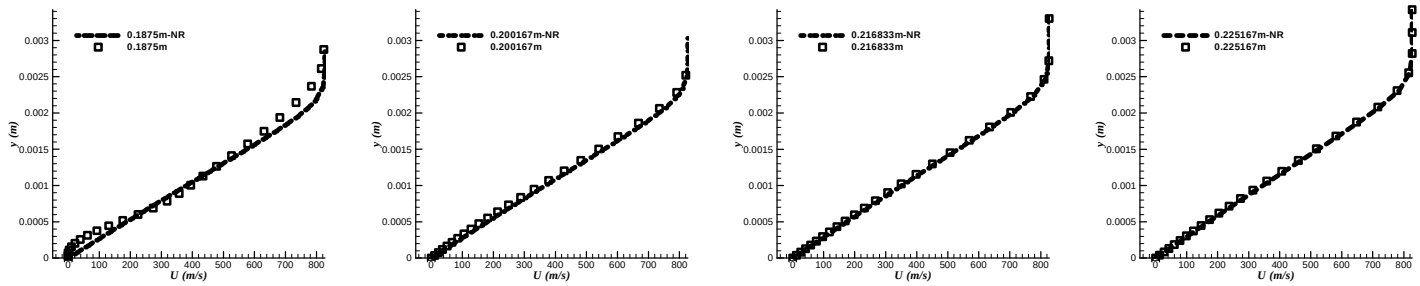

Figure 10.Streamwise velocity profile at different locations upstream of 37.5% roughness compared with no roughness case.

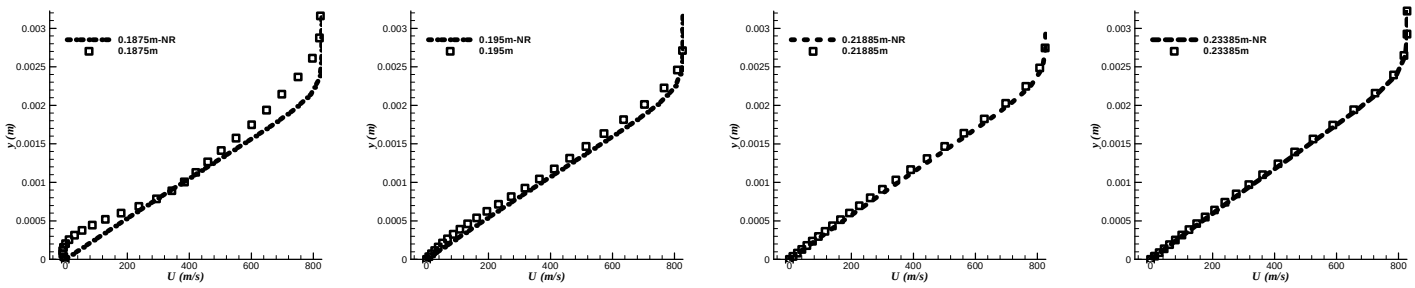

Figure 11.Streamwise velocity profile at different locations upstream of 50% roughness compared with no roughness case.

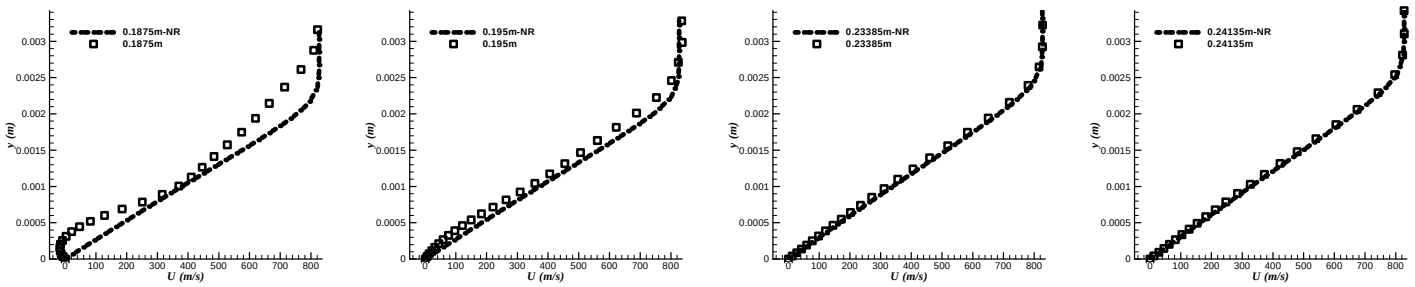

Figure 12.Streamwise velocity profile at different locations upstream of 62.5% roughness compared with no roughness case.

4.3. Stability characteristics of boundary layer without roughness

Stability characteristics of boundary-layer waves of the Mach 5.92 flow is studied by LST using a multi-domain spectral method of Malik [24]. The dimensionless frequency used for linear stability analysis is defined as

$$F = \frac{2\pi f \nu}{u_\infty^2} \tag{14}$$

Where F is dimensionless frequency, ν is kinematic viscous coefficient. In present simulation, $\nu = 6.05\times10^{-5} m^2/s$, $F = 5.30\times10^{-5}$ for the case of $f = 100KHz$ and $u_\infty = 827.29m/s$.

In LST analyses of boundary layer flows, the Reynolds number based on the local length scale of boundary layer thickness δ. They are expressed as

$$R = \frac{\rho_\infty u_\infty \delta}{\mu_\infty}, \delta = \sqrt{\frac{\mu_\infty x}{\rho_\infty u_\infty}} \tag{15}$$

Hence the relation between R and the unit Reynolds number R_∞ is,

$$R = \sqrt{R_\infty x} \tag{16}$$

With the definitions of Reynolds number R and the dimensionless frequency F, the dimensionless circular frequency ω can also be expressed as,

$$\omega = RF \tag{17}$$

Figure 13 shows the eigenvalue spectra of boundary-layer waves at a frequency of $100\,KHz$ at x = 0.189 m. The figure shows wave spectra corresponding to fast acoustic wave, entropy and vorticity waves, and slow acoustic wave. The two discrete waves marked by circles are modes F and S, respectively. Mode F originates from fast acoustic spectrum on the left side of the figure and passes entropy and vorticity spectra at the center as dimensionless frequency increases. Mode S originates from slow acoustic spectrum on the right side of the figure. It becomes unstable in certain range of dimensionless frequency. The figure also shows that mode S at this frequency is unstable at x = 0.189 m with $\alpha_i < 0$.

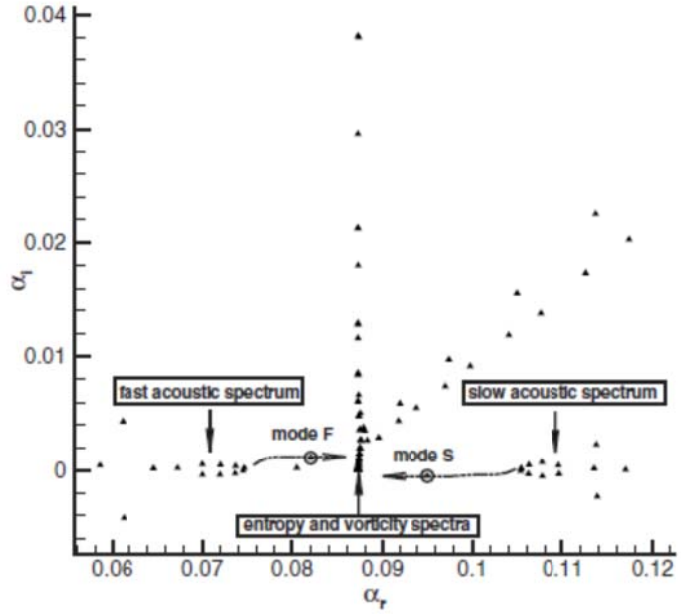

Figure 13. Eigenvalue spectra of boundary-layer waves at the frequency of f=100 kHz at x=0.189 m.

Figure 14 shows phase velocities of boundary-layer waves at two locations of $x = 0.159m$ and $x = 0.189m$ as a function of circular frequency. The three horizontal dashed lines represent phase velocities of fast acoustic wave, entropy and vorticity waves, and slow acoustic wave, respectively. The excellent agreement of phase velocities at two different locations indicates that phase velocity is approximately a function of circular frequency only. The figure clearly shows that mode F originates from fast acoustic spectrum. As ω increases, phase velocity of mode F decreases. When mode F passes entropy and vorticity spectra near $\omega = 0.1$, there exists a jump of phase velocity, which is consistent with theoretical analysis of Fedorov and Khokhlov [25]. On the other hand, mode S originates from slow acoustic spectrum. The figure also shows that mode S synchronizes with mode F at the point of ω_s = 0.11563 and $a_s = 0.93076$.

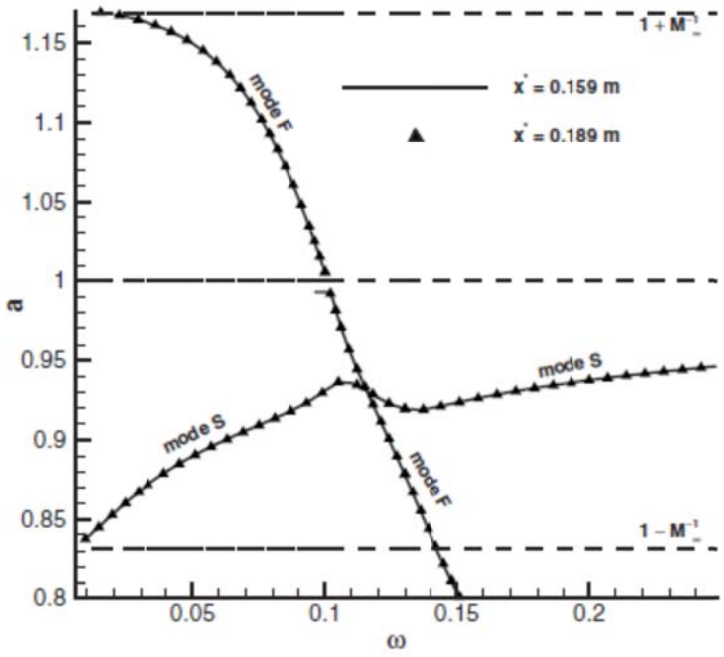

Figure 14. Distributions of phase velocities of boundary-layer waves at two different locations.

Although Figure 14 shows that the synchronization point has a constant value of circular frequency ω_s =0.11563, the location of the synchronization point in x coordinate, x_s, are different for different dimensionless frequencies F. The synchronization location in x coordinate for a given dimensionless frequency can be calculated using the following formula:

$$x_s = \frac{\left(\omega_s / F\right)^2}{\mathrm{Re}_\infty} \tag{18}$$

This equation indicates that the synchronization point moves upstream with dimensionless frequency increasing. Figure 15 shows growth rates of modes F and S at the same set of locations as a function of circular frequency. The horizontal dotted line stands for neutral waves α_i = 0. In Figure 15 the growth rates of either mode S or mode F are approximately functions of circular frequency only. Mode S is unstable in the region from ω_I = 0.00827 to ω_{II} = 0.18465, whereas mode F is always stable. The parameters ω_I and ω_{II} are called branches I and II neutral points of mode S. The locations of branches I and II neutral points in x coordinate, which changes with different dimensionless frequencies, can be calculated by

$$x_I = \frac{\left(\omega_I / F\right)^2}{\mathrm{Re}_\infty}, x_{II} = \frac{\left(\omega_{II} / F\right)^2}{\mathrm{Re}_\infty} \tag{19}$$

Eq. (19) indicates that when non-dimensionalized frequency (F) increases, the corresponding coordinates of branch points decrease. In other words, branches I and II neutral points move upstream when F increases. For wall blowing-suction disturbance at the frequency of $f = 100KHz$, the branch I and the branch II neutral points are located at $0.00678977m$ and $3.384887m$. More results on the LST analysis on the meanflow without roughness can be found in Wang and Zhong's paper [26].

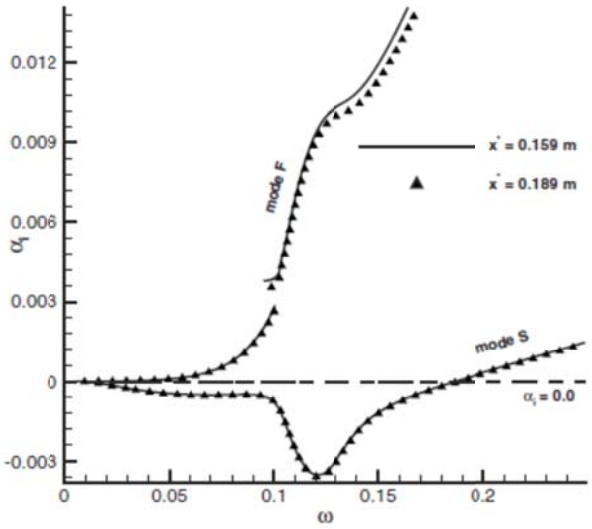

Figure 15. Distributions of growth rates of modes F and S at two different locations..

4.4. The effect of roughness on Mode S perturbation

Mode S perturbation is imposed into the meanflow. In order to study the evolution of the perturbation in streamwise direction, an FFT analysis is performed on the unsteady simulations. Figure 16 (a) and (b) show the growth of mode S pressure perturbation on the wall for case 1 and case 2 respectively. The data for each roughness height is also included on each plot. Here, the symbol h represents the local boundary layer thickness. Since the algorithm of cut cell method doesn't solve for the grid point inside solid region, all perturbation drops back to zero inside the roughness element. That is responsible for the discontinuity in the plot. The roughness of case 1 and case 2 are located upstream of synchronization point at $x_r = 0.1101m$ and $x_r = 0.185m$ respectively. In Figure 16 (a), we can see the perturbation for $0.375h$ roughness is damped a little bit in front of roughness before it starts to grow. The physical explanation for this is not known. However, for all other roughness height, roughness upstream of synchronization point always amplifies perturbation upstream of roughness. The amplification rate depends strongly on the size of roughness. For example, in roughness height $0.25h$ of case 2, the maximum amplitude is just about 3 times the case without roughness. On the other hand, in the biggest roughness case, the jump in perturbation amplitude reaches as high as 13 times without roughness. This amplification in the separation region upstream of roughness agrees with the result by Marxen et al [27].

Downstream of roughness, evolution of perturbation has different trend depending on roughness location. In case 1, perturbation returns to the level as if there is no roughness. However, in case 2 (Figure 16 (b)), roughness height controls how perturbation grows downstream of roughness. It is found that perturbation is amplified for tall roughness ($0.5h$ and $0.625h$). For small roughness, perturbation remains the same as no roughness case. In general, roughness element at this location has more pronounced amplification effect in the vicinity upstream of roughness than downstream. Moreover, if roughness is placed too upstream of synchronization point, roughness tends to have very small effect on modal growth.

As roughness moves closer to the synchronization point in case 3 and case 4, we observed different trend for the growth of pressure perturbation. In Figure 16 (c), the roughness sits at exactly the synchronization point of the perturbation frequency. The perturbation for the smallest roughness, $0.25h$, is still amplified and grows downstream as if there is no roughness. However,

for taller roughness, perturbation only grows in far upstream region. As the perturbation gets closer to the roughness, it starts to be damped suddenly. The location where the damping starts depends on roughness height. In $0.375h$ case, damping starts at around $x = 0.317m$. When roughness height is increased to $0.5h$, the onset of damping moves to around $x = 0.309m$. Further increase roughness height to $0.625h$ moves it to even more upstream $x = 0.303m$. In the region between the onset of damping and roughness, strong modulation of different modes is observed. Since modulation does not exist for the case without roughness, the modes which interact with the imposed mode must be generated by the roughness. Downstream of the roughness, perturbation in small roughness case ($0.25h$) follows the trend as no roughness case. On the other hand, perturbation is highly damped in tall roughness cases. The bigger the roughness is, the weaker pressure perturbation is compared with the case without roughness. Tall roughness in the location acts as a perturbation damper of the imposed mode instead of an amplifier like in case 1 and case 2.

In the final test case, the roughness is moved to even further downstream to $x = 0.410m$, which is behind the synchronization point of the imposed frequency. Figure 16 (d) shows how pressure perturbation interacts with different roughness height at this location. Similar to case 3, perturbation is amplified far upstream of roughness, but is all damped when it gets close to the vicinity of roughness. One difference between this case and case 3 is for all roughness height, damping effect is observed. In addition, the location of the onset of damping moves to more upstream than in case 3. In the region behind roughness, perturbation for all cases stays on the same level and does not grow at all, which is significantly different from case 3. Judging from this result, we can say that roughness in this location acts as a more effective perturbation damper of the imposed mode than in case 3, which can potentially stabilize the flow.

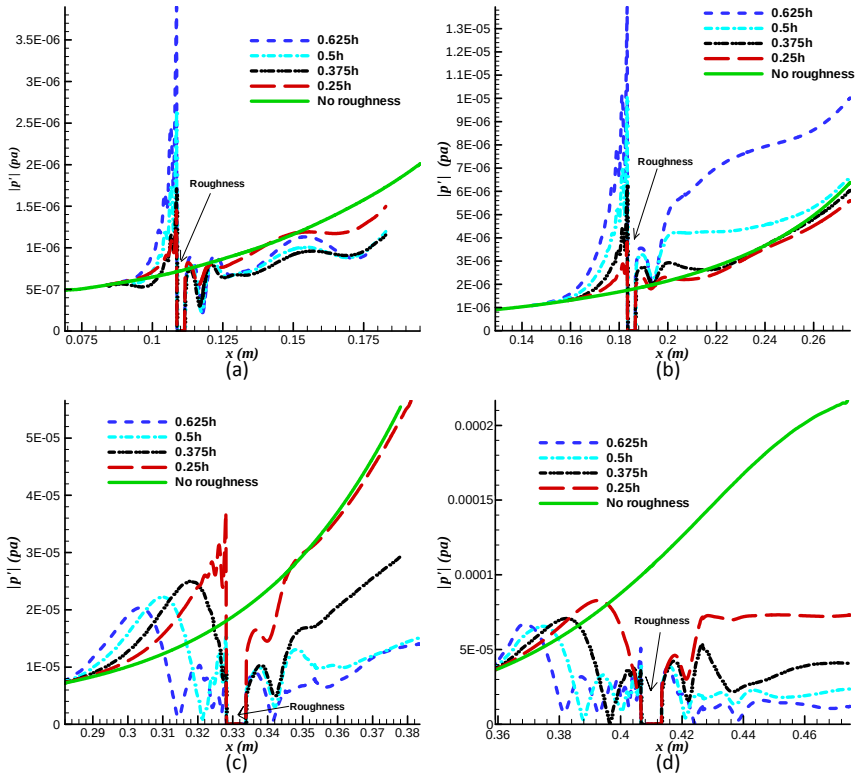

Figure 16. Evolution of Mode S pressure wall-perturbations with different roughness height. (a) case1 roughness at x=0.1101m (b) case 2 roughness at 0.185m (c) case 3 roughness at 0.331m (d) case 4 roughness at 0.410m

4.5. The effect of roughness on the perturbation of different frequencies

In our previous study [20], perturbation mode corresponding to mode S and mode F at $100KHz$ have been imposed into the meanflow separately. In this paper, it is of interest that how roughness affects disturbance at different frequency. Therefore, a perturbation with a wide range of frequency is also imposed into the meanflow. An example of such perturbation is a Gaussian shape pulse perturbation. A hole is modeled on the flatplate located at $x = 0.1m$ with a width of $0.003m$. The hole introduces wall normal velocity in the flow. At each grid point, the perturbation is Gaussian in time, as shown in Figure 17(a). However, in order not to introduce any additional mass into the meanflow, the perturbation is sinusoidal in space as shown in Figure 17(b).Figure 17(c) shows the FFT spectrum of the perturbation. It can be seen that the pulse has a frequency range around $1MHz$, which is broad enough to cover the most unstable modes in the flow.

This pulse model is implemented into the meanflow of case 2 in which roughness locates at $x = 0.185m$. Figure 18 shows the pressure perturbation contour resulted from the pulse for 50% boundary layer thickness roughness case. The hole and roughness are also shown. Figure 19 shows the pressure perturbation at different locations. It is seen that besides the excited perturbation on the wall region. The wall normal velocity pulse has also created perturbation outside of boundary layer. However, this perturbation is weak and it decays fast outside of boundary layer. The pulse also excites the flow inside the boundary layer and creates pressure perturbation on the wall with pattern similar to mode S or mode F in the previous section. Yet this perturbation is not periodic due to the Gaussian shape of the pulse. Figure 20 shows the time history of pressure wall perturbation at various streamwise locations upstream of 50% boundary layer roughness. Initially, the front part of the wave pack is amplified as it travels closer to the roughness. Meanwhile, the tail part is slightly damped. When the wave pack travels further, for example at $0.18285m$, the front part is also damped while the tail part is highly damped. Since this pulse comprises a wide range of frequency, an FFT analysis is performed to get a better understanding of the relation between roughness and perturbation frequency. Figure 21 shows the frequency spectra of the pulse at the same locations as in Figure 20. The results for both with roughness and without roughness are included. The location of roughness in this case, $x = 0.185m$, corresponds to the location of synchronization point for perturbation at frequency $133.26KHz$ which is highlighted in Figure 21(a). It is seen that in the upstream region of roughness, perturbations at frequency from $0Hz$ to $120KHz$ are amplified compared with the no roughness case. Moreover, the peak observed in Figure 21(b) around $f = 165KHz$ has switched to a lower frequency region around $f = 125KHz$ at $x = 0.17385m$ with roughness. This shift can be explained by the increase of boundary layer thickness due to existence of roughness. Since the wavelength of second mode is related to the boundary layer thickness, a thicker boundary layer produces a longer second mode wavelength and thus the frequency becomes lower. This result also agrees with Marxen et al [27] in which states that roughness can move the second mode instability to lower frequency region. At $x = 0.18285m$, the perturbation arrives at a location just upstream of roughness. It can be seen that the perturbation at frequency around $f = 133.26KHz$ ($116KHz$ to $155KHz$) is strongly damped. The lowest part of the FFT result is at $f = 140KHz$, which is very close to the synchronization point frequency.

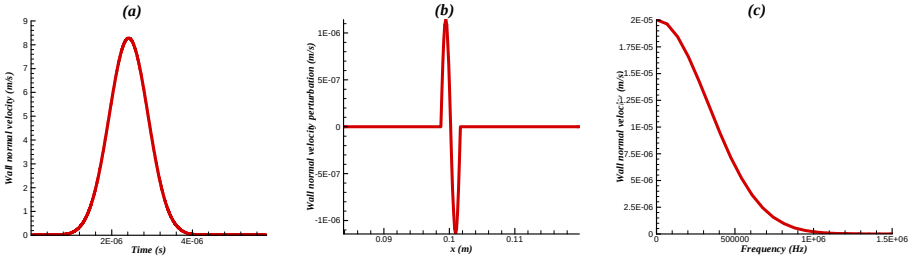

Figure 17.(a) Time history of wall normal velocity on the wall. (b) Snapshot of wall normal velocity in space. (c) FFT result of the Gaussian shape perturbation in (a).

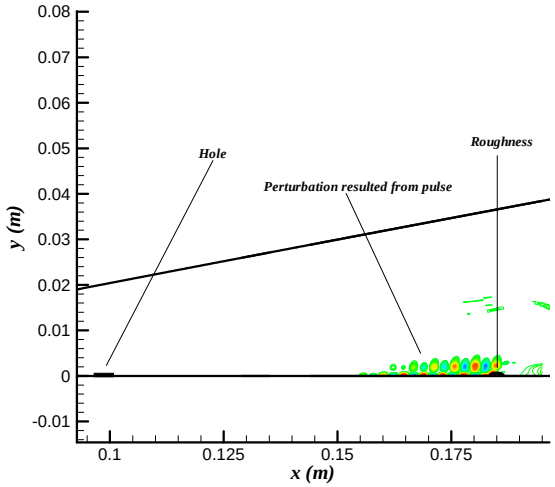

Figure 18. Schematic presentation of numerical setup for the pulse case; the hole to introduce perturbation, roughness and pressure perturbation are shown.

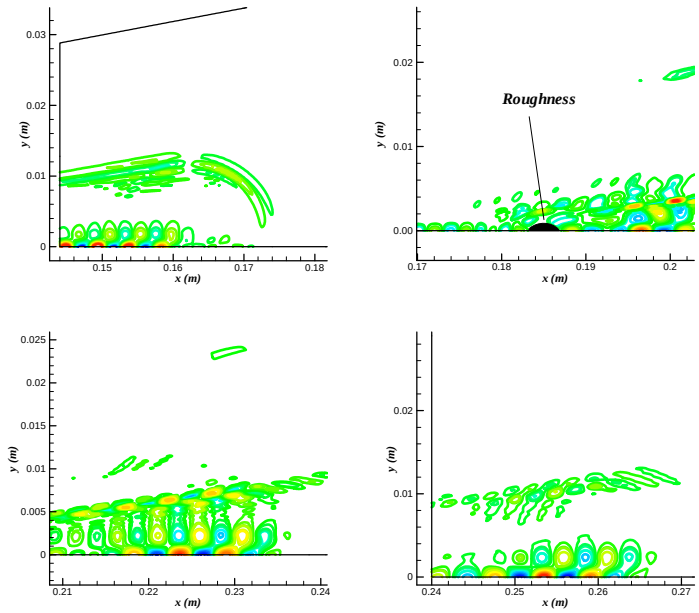

Figure 19. Pressure perturbation contour at different location

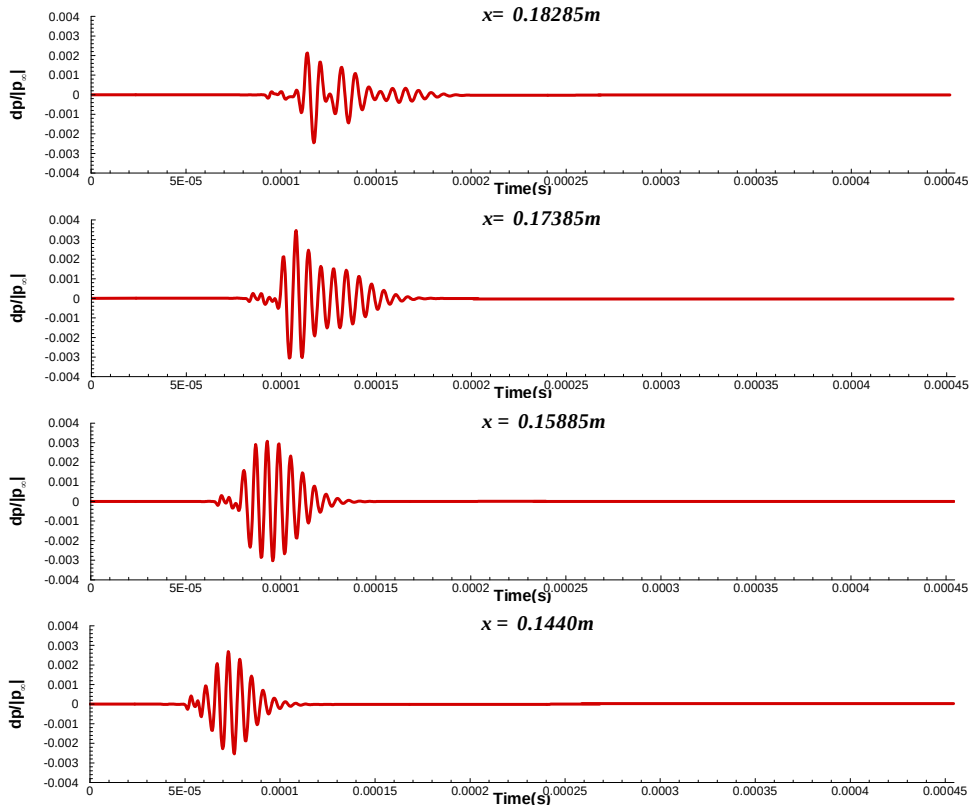

Figure 20.Time history trace of pressure wall-perturbations at various streamwise locations at the upstream part of roughness.

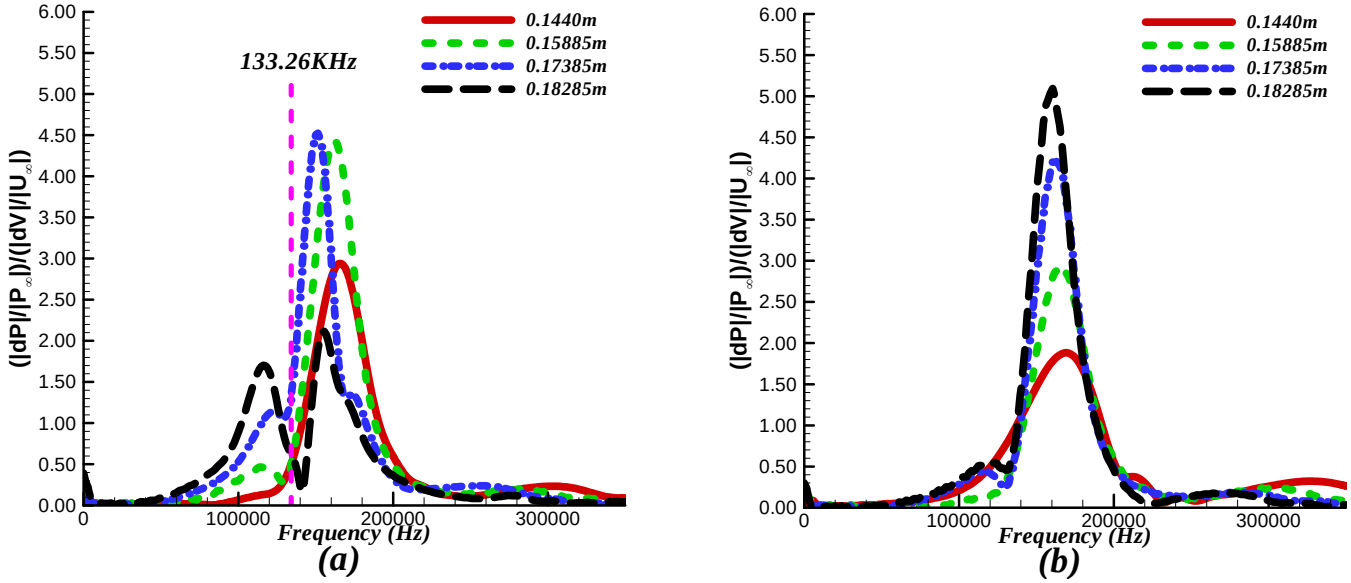

Figure 21. Non-dimensional frequency spectra of wall pressure perturbation at different location. (a) Upstream of roughness (b) No roughness case

Figure 22 shows time history of wall perturbation at different x location behind the roughness. The front part of the wave starts to grow again once it has passed the roughness. However, the tail part still exhibits some sort of damping effect due to the roughness. At $x = 0.21735m$, the tail part of the wave has reached its lowest amplitude and it starts to grow thereafter. The growth at the tail part has become stronger than the front part after it has reached it minimum. A detail FFT analysis on such perturbation is shown in Figure 23(a). Figure 23(b) shows the FFT results of the same locations without roughness. At $x = 0.19635m$, a location just behind the roughness, perturbation at frequency around $120KHz$ to $100KHz$ is amplified compared with no roughness. However, frequencies around $133.26KHz$ are all highly damped. The frequency range of this damping effect is from around $120KHz$ to $170KHz$. It can also be seen that the strongest damping occurs very close to the synchronization point frequency. As the perturbation travels downstream, the high frequency perturbation (around $140KHz$ to $170KHz$) that has been damped in the previous location drops even further. Meanwhile, perturbation at frequency around $133.26KHz$ starts to grow at a slow rate. For the amplified perturbation at frequency around $120KHz$, the growth is very strong, and the perturbation amplitude is always greater than the no roughness case. The FFT results from upstream and downstream of roughness shows that a two dimensional roughness is capable of amplifying perturbation at frequency lower than the synchronization frequency, while it damps frequency close to and higher than the synchronization frequency.

Figure 24 shows the normalized amplitude of wall pressure perturbation at three different frequencies. In particular, we are interested in the frequencies higher than, close to and lower than the synchronization point frequency $133.26KHz$. Therefore, $120KHz$ $130KHz$ and $140KHz$ are chosen. For comparison, their evolution in the case without roughness is also included. It can be clearly seen that at $120KHz$, perturbation is highly amplified due to the roughness. At the end of the figure, its amplitude is almost twice than the case without roughness. This trend is very similar to the one obtained for our mode S case 2 shown in Figure 16 (b) .However, perturbation at $130KHz$, which is close to the synchronization frequency, is damped compared with no roughness. Without roughness, perturbation at this frequency grows exponentially and it reaches normalized amplitude almost 4 at the end of the figure. With roughness, this perturbation is amplified a little bit far upstream of roughness. As it gets closer to the roughness, it starts to be damped significantly. Its normalized amplitude only reaches about 2.5 at the end of the figure. This result compares very well with the mode S case in which roughness is placed at the synchronization point as shown in Figure 16 (c). For perturbation at $140KHz$, the damping effect is even more pronounced than the previous case. As shown in Figure 24 (c), its normalized amplitude grows to around 8 without roughness. On the other hand, with the existence of roughness, the amplitude level stays at around 2 at the end of the figure. Again, this result agrees very well with our mode S case 4 which roughness is placed downstream of synchronization point as shown in Figure 16 (d).

The agreement between results obtained from the pulse case and mode S case can be explained by the analogy of imposing different frequencies and changing roughness location. Equation (18) implies the position of synchronization point is inverse proportion to non-dimensional frequency. Therefore, roughness at different location corresponds to the synchronization points of different frequencies. Namely, an upstream location corresponds to the synchronization point of high frequency. In our mode S case, four different roughness locations have been considered but only one frequency of perturbation is imposed. The results show that upstream of synchronization point for the perturbation frequency, the perturbation is amplified. However, as roughness is placed close to or downstream of synchronization point, the perturbation is damped. In the pulse case, roughness location is fixed. Instead, perturbation of a wide range of frequency is imposed. Therefore, the location of roughness is the synchronization point of one particular frequency ($133.26KHz$) in this case. In the view of perturbation which frequency is below $133.26KHz$, the roughness location is the same as upstream of its synchronization point. As a result, the amplified perturbation at around $120KHz$ is consistent with the previous conclusion. On the other hand, in the view of perturbation which frequency is higher than $133.26KHz$, the roughness location is located downstream of its synchronization points. The damping effect observed for $140KHz$ supports the previous conclusion as well. This agreement solidifies our findings.

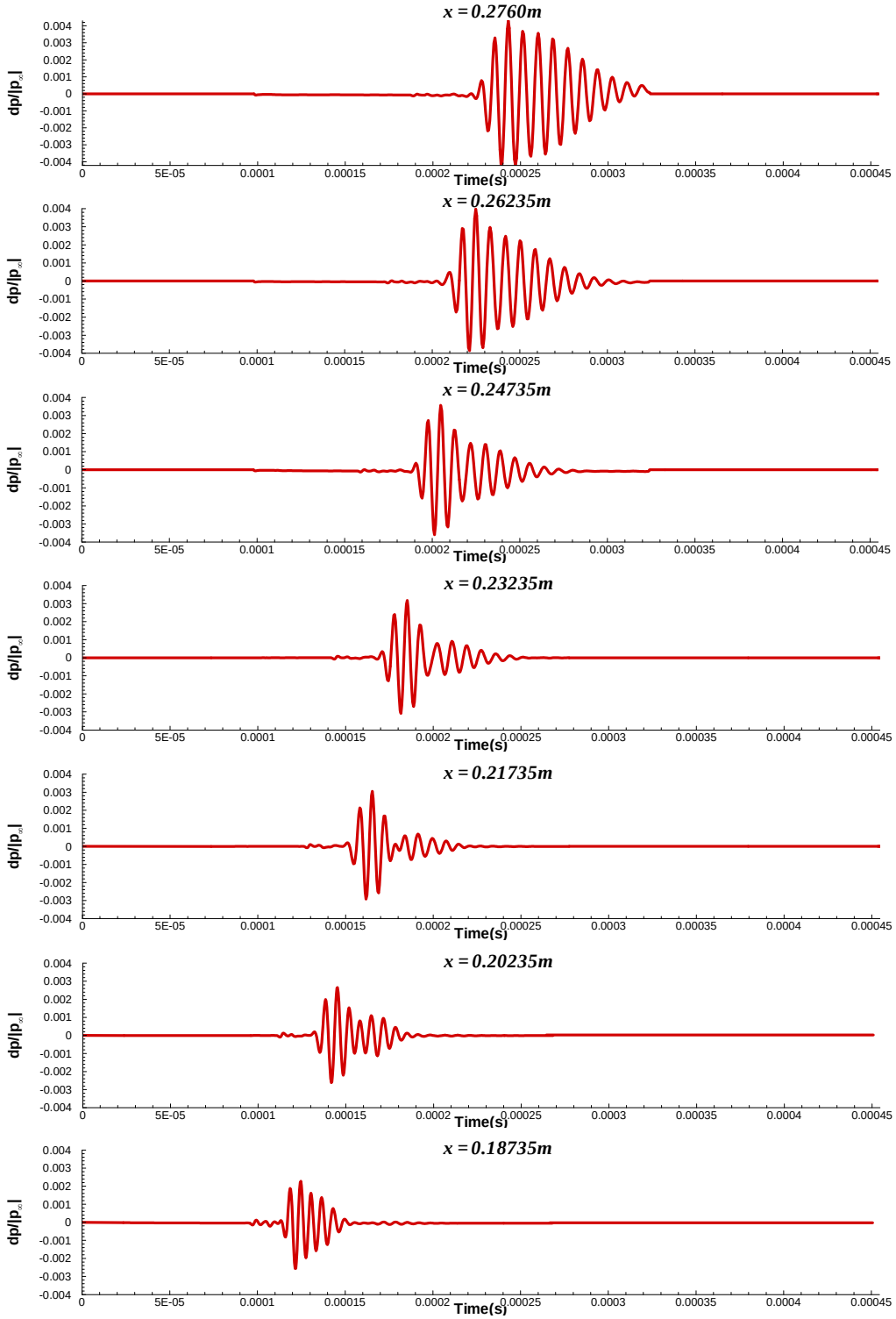

Figure 22.Time history trace of pressure wall-perturbations at various streamwise locations at the downstream part of roughness.

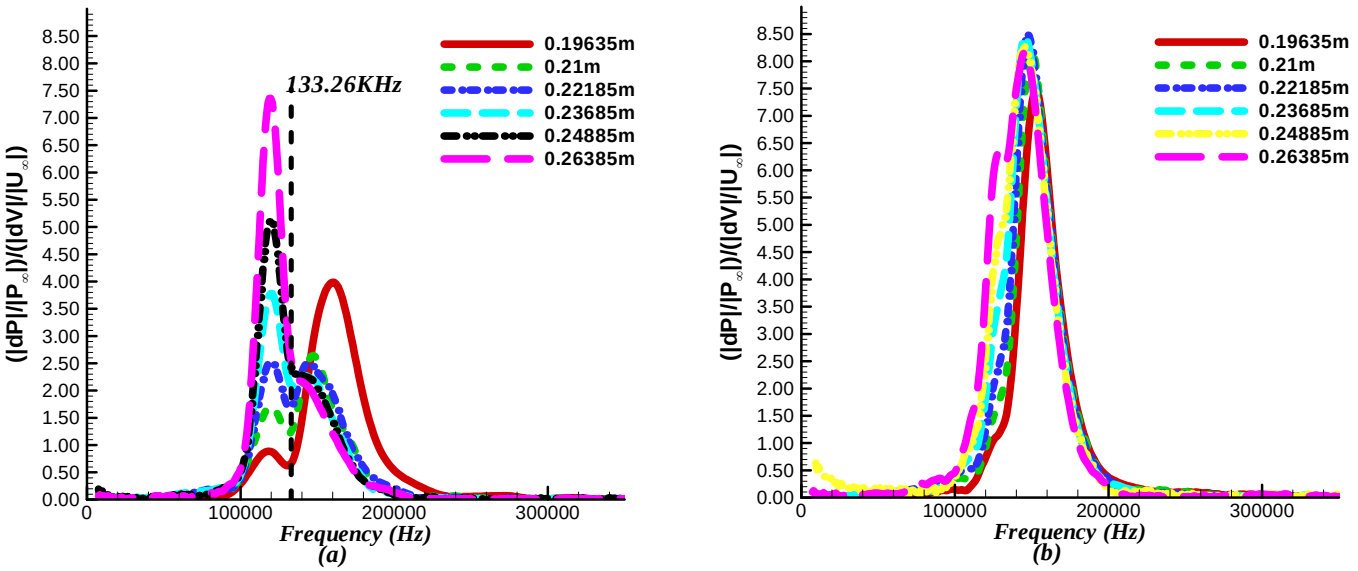

Figure 23. Non-dimensional frequency spectra of wall pressure perturbation at different location. (a) Downstream of roughness (b) No roughness case

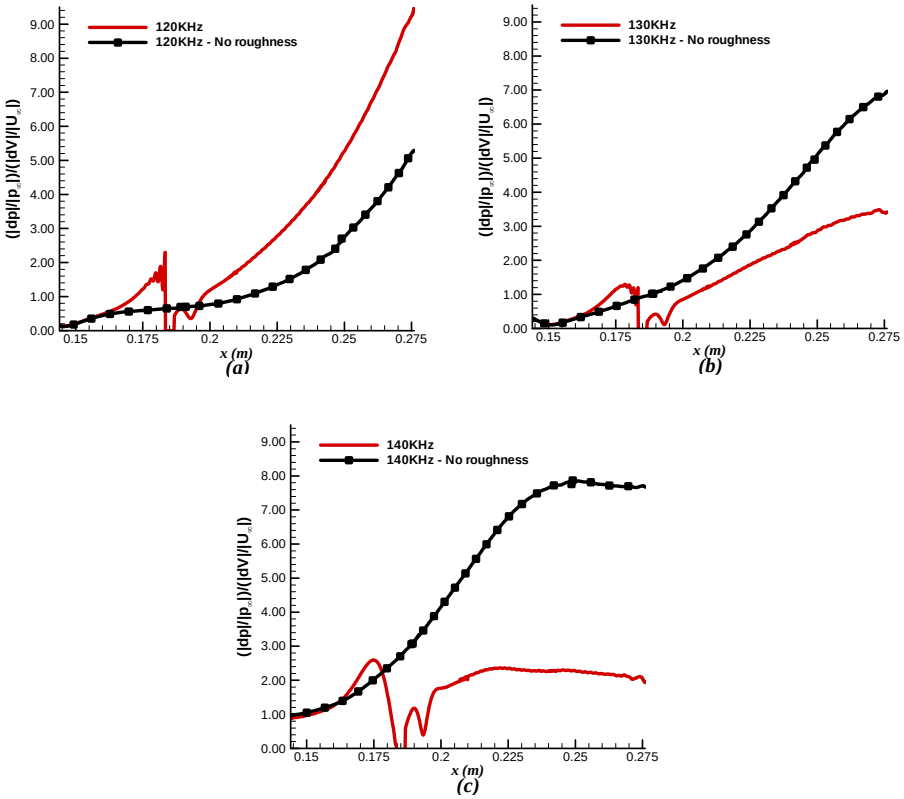

Figure 24. Spatial evolution of wall pressure perturbation at three different frequencies (a) 120 KHz (b) 130 KHz (c) 140 KHz

4.6. The effect of two roughness elements

Other than one single roughness, a two roughness model is also considered. The first roughness is at the same location as case 2, x_r=0.185 m. The first roughness height is fixed at 50% local boundary layer thickness. The second roughness is put in the downstream region of first roughness at x_r=0.231 m, while its height is kept the same as the first roughness. The location of first roughness corresponds to the synchronization point of frequency $133.26KHz$, while the location of the second roughness corresponds to the synchronization point of frequency $119.26KHz$.

Figure 25 shows the pressure contour of the two roughness meanflow. It is seen that the second roughness generated the same Mach wave as one roughness case. Moreover, the wave pattern looks very similar to that for the first roughness. In unsteady simulation, the same pulse model mentioned in the section 4.5 is implemented into this meanflow. Therefore, the perturbation would have a frequency range of 1MHz as in Figure 17. The pressure perturbation contour is shown in Figure 26. Similar to one roughness case, it is of interest to study how the perturbation interacts with the two roughness elements. Figure 27 shows the spatial development of perturbation at different frequency. Same as in Figure 24, the frequency chosen are $120KHz$, $130KHz$ and $140KHz$. Since the location of the second roughness corresponds to the synchronization point of frequency $119.26KHz$, it is expected the perturbation at these three frequencies will be damped after the second roughness. Figure 27 confirms the expectation. It is shown that the first roughness amplifies $120KHz$ perturbation since it is upstream of its synchronization point. However, when the perturbation travels downstream and approaches the second roughness, it starts to be damped since the roughness locates very close to its synchronization point. Downstream of the second roughness, the perturbation at $120KHz$ is weaker than the case without roughness. On the other hand, both roughness are located downstream of their synchronization point for perturbation at frequency $130KHz$ and $140KHz$. Therefore, the two roughness elements have damping effect on these two frequencies. Figure 27 (b) and (c) show this trend. It is seen that the damping effect is more pronounced in two roughness case than in one roughness as seen in Figure 27.

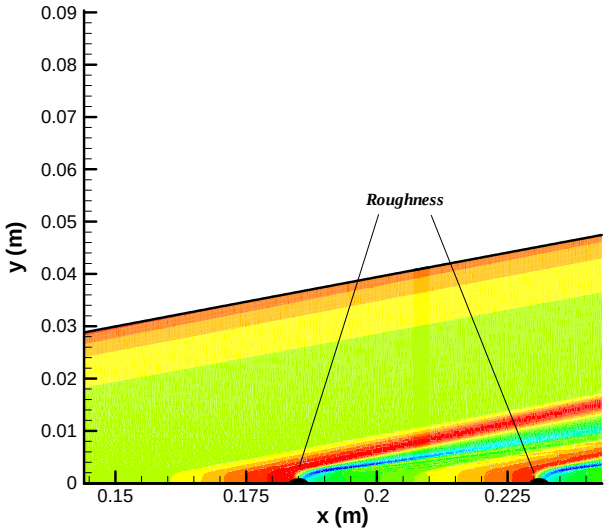

Figure 25. Pressure contour of two roughness meanflow.

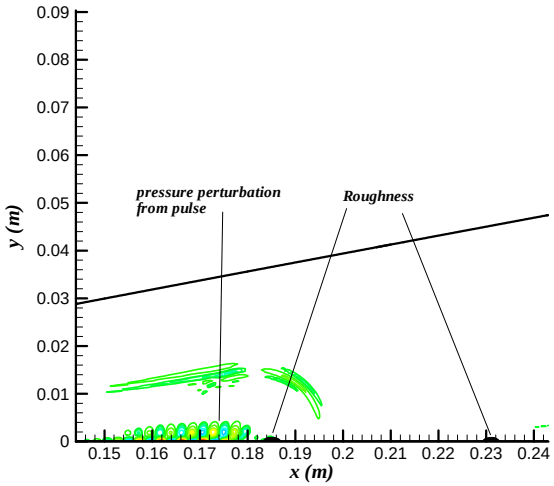

Figure 26. Pressure perturbation contour for two roughness case.

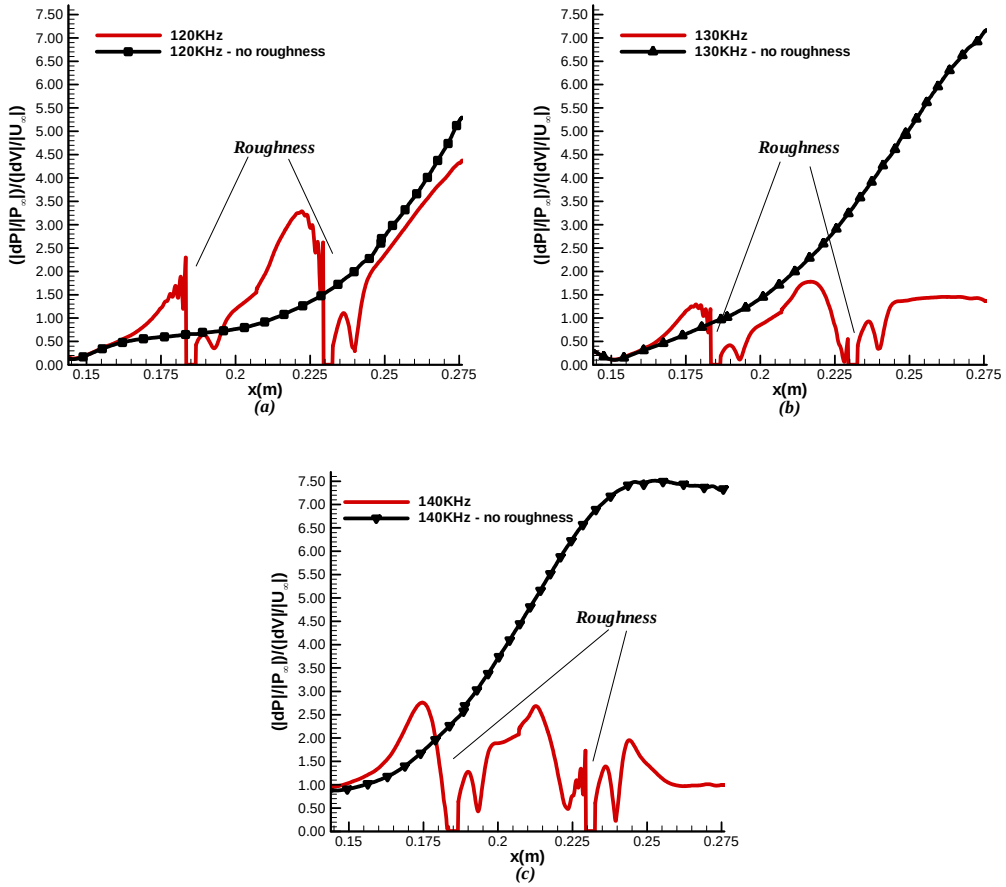

Figure 27. Spatial evolution of wall pressure perturbation for two roughness case at three different frequencies (a) 120 KHz (b) 130 KHz (c) 140 KHz

5. Conclusion

In this paper, we have further investigated the effect of two dimension roughness on modal growth of perturbation with a wide frequency spectrum on a hypersonic flatplate at Mach 5.92. Both one roughness element case and two roughness elements case have been studied. The steady flow is simulated by solving compressible Navier-Stokes equation. In unsteady simulation, a wall normal velocity pulse is modeled and imposed into the meanflow. Our results confirmed our previous finding in Duan et al, and Fong et al [18, 20] that roughness is capable of amplifying perturbation at certain frequency if roughness is placed upstream of the synchronization point of a particular frequency. Meanwhile, if roughness is place downstream of the synchronization point of a frequency, the perturbation which has higher frequency will be damped. The agreement between mode S case and pulse case solidified our conclusion. This finding can provide an explanation of roughness delay transition as shown in some experiments [16, 17]. Moreover, using this information can also give us a new way to control boundary layer transition by using two dimensional surface roughness. In the future, we will extend our study from two dimensions to three dimensional roughness effect.

Acknowledgments

This work was sponsored by the Air Force Office of Scientific Research, USAF, under AFOSR Grant #FA9550-07-1-0414, monitored by Dr. John Schmisseur. This work was also sponsored by the AFOSR/NASA National Center for Hypersonic Research in Laminar-Turbulent Transition. The views and conclusions contained herein are those of the author and should not be interpreted as necessarily representing the official policies or endorsements either expressed or implied, of the Air Force Office of Scientific Research or the U.S. Government.

References

1. Schneider, S.P., *Summary of hypersonic boundary-layer transition experiments on blunt bodies with roughness, J. Spacecraft and Rockets.* Journal of Spacecraft and Rockets, 2008. **45**: p. 1090-1112.
2. Board, D.S., *Final report of the second defense science board task force on the national aero-space plane (NASP)*. 1992. p. 94-00052.
3. Anderson, J.D., *Hypersonic and high temperature gas dynamics*. 2000: AIAA.
4. Berry, S., Horvath, T., *Discrete roughness transition for hypersonic flight vehicles*, in *45th AIAA Aerospace Sciences Meeting and Exhibit*. 2007: Reno, Nevada.
5. Saric, W.S., Reed, H. L., and Kerschen, E. J., *Boundary-Layer Receptivity to Freestream Disturbances.* Annual Review of Fluid Mechanics, 2002. **34**: p. 291-319.
6. Mack, L.M., *Boundary layer linear stability theory*, in *AGARD Report*. 1984. p. 1-81.
7. Maslov, A.A., Shiplyuk, A. N., Sidorenko, A., and Arnal, D., *Leading-edge Receptivity of a Hypersonic Boundary Layer on a Flat Plate.* Journal of Fluid Mechanics, 2001. **426**: p. 73-94.
8. Maslov, A.A., Mironov, S. G., Shiplyuuk, A. A., Sidorenko, A. A., Buntin, D. A., and Aniskin, V. M., *Hypersonic Flow Stability Experiments.* 2002. **AIAA 2002-0153**.
9. Demetriades, A., *Hypersonic Viscous Flow Over A Slander Cone. Part III: Laminar Instability and Transition.* AIAA paper 74-535, 1974.
10. Demetriades, A., *Laminar Boundary Layer Stability Measurements at Mach 7 Including Wall Temperature Effects.* AFOSR-TR-77-1311, 1977.
11. Malik, M.R., Lin, R. S., and Sengupta, R., *Computation of Hypersonic Boundary-Layer Response to External Disturbances.* AIAA paper 1999-0411, 1999.
12. Ma, Y., and Zhong, X., *Receptivity to Freestream Disturbances of Mach 8 Flow over A Sharp Wedge.* AIAA paper 2003-0788, 2003.
13. Wang, X., Zhong, X., and Ma, Y., *Response of a hypersonic boundary layer to wall blowing - suction.* AIAA Journal, 2011. **In press**.
14. Balakumar, P. *Transition In a Supersonic Boundary-Layer Due To Roughness Aand Acoustic Disturbances*. in *AIAA*. 2003.
15. Marxen, O., Iaccarino, G., *Numerical simulation of the effect of a roughness element on high-speed boundary-layer instability*, in *38th Fluid Dynamics Conference and Exhibit*. 2008: Seattle, Washington.

16. Holloway, P.F.a.S., J.R., *Effect of controlled surface roughness on boundary-layer transition and heat transfer at Mach numers of 4.8 and 6.0*. 1964, NASA.
17. Fujii, K., *An Experiment of Two Dimensional Roughness Effect on Hypersonic Boundary-Layer Transition*, in *43rd AIAA Aerospace Sciences Meeting and Exhibit*. 2005: Reno, Nevada USA.
18. Duan, L., Wang, X., and Zhong, X., *A High-Order Cut-Cell Method for Numerical Simulation of Hypersonic-Boundary Transition with Arbitrary Surface Roughness.* AIAA paper 2009-1337, 2009.
19. Duan, L., Wang, X., and Zhong, X., *Stability of a Mach 5.92 Flat-Plate Boundary Layer with the Effect of 2-D Finite Height Roughness.* AIAA Journal (To be appear in 2012), 2012.
20. Fong, K., Wang, X. and Zhong, X., *Finite roughness effect on modal growth of a hypersonic boundary layer*, in *50th AIAA Aerospace Sciences Meeting Including the New Horizons Forum and Aerospace Exposition*. 2012: Nashville, Tennessee, USA.
21. Duan, L., Wang, X., and Zhong, X. , *A high-order cut-cell method for numerical simulation of hypersonic boundary-layer instability with surface roughness.* Journal of Computational Physics, 2010. **229**(19): p. 7207-7237.
22. Whitehead, A.H., *Flow field and drag characteristics of several boundary-layer tripping elements in hypersonic flow.* Techinical paper, NASA, 1969. **5454**.
23. Klebanoff, P.S., *Mechanism by Which a Two-Dimensional Roughness Element Induces Boundary-Layer Transition.* The Physics of Fluids, 1972. **15-7**: p. 1173-1188.
24. Malik, M.R., *Numerical methods for hypersonic boundary layer stability.* Journal of Compuational Physics, 1990. **86**(2): p. 376 - 413.
25. Fedorov, A.V., and Khokhlov, A. P., *Prehistory of Instability in a Hypersonic Boundary Layer.* Theoretical and Computational Fluid Dynamics, 2001. **14**: p. 359-375.
26. Wang, X., and Zhong, X., *Effect of wall perturbations on the receptivity of a hypersonic boundary layer.* Physics of fluids, 2009. **21** (044101).
27. Marxen, O., Iaccarino, G. and Shaqfeh,E.S.G., *Disturbance evolution in a Mach 4.8 boundary layer with two-dimensional roughness-induced separation and shock.* Journal of Fluid Mechanics, 2010. **648**: p. 435-469.